Journal of Manufacturing Processes 30 (2017) 41–50

Contents lists available at ScienceDirect

Journal of Manufacturing Processes

journal homepage: www.elsevier.com/locate/manpro

Technical Paper

Analytical solutions for fixed-free beam dynamics in thin rib machining

Tony L. Schmitz*, Andrew Honeycutt

UNC Charlotte, Department of Mechanical Engineering and Engineering Science, 9201 University City Blvd., Charlotte, NC 28223, United States

ARTICLE INFO

Article history:
Received 17 July 2017
Received in revised form 29 August 2017
Accepted 3 September 2017

Keywords:
Dynamics
Beam
Rib
Milling
Receptance coupling

ABSTRACT

Two different analytical approaches for predicting thin rib, fixed-free beam dynamics with varying geometries are presented. The first approach uses the Rayleigh method to determine the effective mass for the fundamental bending mode of the stepped thickness beams and Castigliano's theorem to calculate the stiffness both at the beam's free end and at the change in thickness. The second method uses receptance coupling substructure analysis (RCSA) to predict the beam receptances (or frequency response functions) at the same two locations by rigidly connecting receptances that describe the individual stepped beam sections, where the receptances are derived from the Timoshenko beam model. Comparisons with finite element calculations are completed to verify the two techniques. It is observed that the RCSA predictions agree more closely with finite element results. Experiments are also performed, where the stepped beam thickness is changed by multiple machining passes, and receptance measurements are carried out between passes. The RCSA predictions are compared to experimental results for natural frequency and stiffness. Agreement in natural frequency to within a few percent is reported.

1. Introduction

It is common practice to produce monolithic metallic components with thin ribs from solid billets by machining (subtractive manufacturing). This enables complex parts with high strength-to-weight ratio to be produced without significant assembly time and cost. Application domains range from aerospace structures to laptop cases. With the recent advances in metal additive manufacturing, it is also possible to produce near net shape parts that require only minimal machining to provide the desired surface finish and dimensional accuracy. This is particularly attractive for titanium alloys due to their high material cost and low machinability. The inherent challenge with this hybrid (i.e., combined additive and subtractive) approach is machining flexible parts. The low dynamic stiffness of the thin, near net shape ribs limits both machining stability (i.e., self-excited vibration, or chatter, can occur) and part accuracy (via the surface location errors that can arise from forced vibrations) [1].

Because thin rib machining is widespread, many authors have reported modeling efforts and production strategies with the intent to improve process performance. These efforts are summarized in Table 1. While this review may not be exhaustive, it does demonstrate the significant effort that has been expended on this important technological challenge over the past two decades.

In prior work, finite element analysis has been the primary tool to model and predict the thin rib dynamics and, in many cases, the change in the rib dynamics as material is removed. In this paper, two analytical approaches are presented to describe the stiffness and natural frequency of fixed-free beams, as well as the change in stiffness and natural frequency as material is removed by milling. The specific challenge of near net shape machining, where an initially thin rib is machined to produce a thinner rib, is addressed. The advantage of an analytical approach to the system dynamics prediction is that, as the dynamics change, the machining conditions can be selected and updated at less computational expense than a full finite element solution to maximize material removal rate for the current dynamic system. Naturally, these operating parameters change as material is removed (as evidenced by the prior research efforts), so an analytical updating procedure is beneficial.

In this analysis fixed-free beams with stepped profiles are used to represent the thin ribs geometries and subsequent material removal. The paper outline follows.

- First, the two analytical models are described. Rayleigh's method is applied to determine the effective mass and Castigliano's theorem is used to find the stiffness. Together, the mass and stiffness

* Corresponding author.
E-mail address: tony.schmitz@uncc.edu (T.L. Schmitz).

http://dx.doi.org/10.1016/j.jmapro.2017.09.002
1526-6125/

Table 1
Prior research in thin rib machining.

First author	Year	Ref.	Topic
Y. Altintas	1995	[2]	The authors considered the influence of plate dynamics on the geometric accuracy of machined thin ribs.
J. Tlusty	1996	[3]	Techniques for machining thin ribs using relieved shank tooling in a series of axial passes, finishing the rib on every pass, was described.
S. Smith	1998	[4]	Tool path strategies for the machining of thin webs which rely on the support of the unmachined workpiece were investigated.
H. Ning	2003	[5]	Finite element thin rib part models were used to assess dimensional accuracy during milling.
S. Ratchev	2004	[6]	Force-induced geometric errors were predicted in thin rib machining using finite element analysis and a voxel-transformation model.
S. Ratchev	2004	[7]	An adaptive theoretical force-finite element analysis deflection model was used to predict thin rib surface errors during milling.
U. Bravo	2005	[8]	A three-dimensional stability lobe diagram was presented that considered both the part and tool frequency response functions, as well as the intermediate stages of the rib machining.
S. Ratchev	2005	[9]	Finite element models were used to predict and compensate force-induced geometric errors in machining of thin rib structures.
V. Thevenot	2006	[10]	A three-dimensional stability lobe diagram was presented that incorporated the spatial variation in the thin rib dynamics. Modal testing and finite element analysis were used to identify the thin rib frequency response functions.
I. Mañé	2008	[11]	A spindle-tool finite element model that considered the gyroscopic moment of the spindle rotor and the speed-dependent bearing stiffness was coupled to a finite element model of the thin rib part to predict milling stability.
J.K. Rai	2008	[12]	A finite element-based milling process plan verification model was presented. The effects of fixturing, operation sequence, tool path, and operating parameters were considered to predict the thin rib part deflections.
S. Seguy	2008	[13]	The authors examined the relationship between chatter instability and surface roughness for thin rib milling. Finite element models were used to describe the rib dynamics.
O.B. Adetoro	2009	[14]	Finite element and experimental frequency response functions were used to obtain stable operating parameters for thin rib machining.
W. Chen	2009	[15]	The authors considered the effect of machining deformation that occurs in the current layer on the nominal cutting depth in the next layer during thin rib milling.
L. Gang	2009	[16]	Three-dimensional finite element models of a helical tool and a thin titanium alloy (6Al–4 V) cantilever were used to predict the cutting deformation during milling.
L. Arnaud	2011	[17]	Finite element analysis was used to model the part and time domain simulation was used to predict the thin rib machining stability.
R. Izamshaw	2011	[18]	A combination of finite element and statistical analyses were used to predict part deflection during thin rib machining.
S. Smith	2012	[19]	Sacrificial structure preforms that support the part during machining, but are not a part of the finished component, were designed and tested.
A. Polishetty	2014	[20]	The trochoidal milling strategy was used for thin rib machining of titanium alloy 6Al–4 V.

give the natural frequency. Receptance coupling substructure analysis (RCSA) is also implemented to rigidly attach the two sections of the rib: a thicker base and thinner free end. This represents the beam geometry as material is removed and a section of the profile changes. The RCSA calculations predict the assembly receptance (or displacement-to-force frequency response function); the fundamental natural frequency and corresponding modal stiffness are extracted from the predicted receptance. In both cases, comparisons to finite element analysis calculations are presented.

- Second, the experimental setup and approach are described.
- Third, a comparison between experiments and RCSA predictions is provided.
- Fourth, conclusions are presented.

2. Analytical models

2.1. Raleigh method

The maximum kinetic energy for the free vibration of a continuous (distributed mass) beam can be expressed as:

$$T_{max} = \frac{1}{2} m_{eff} \dot{y}_{max}\, 2, \tag{1}$$

where m_{eff} is the effective mass for the fundamental mode of vibration and $\dot{y}_{max}$ is the maximum beam velocity in the lateral direction (perpendicular to the beam axis) [21]. For harmonic motion, the displacement can be expressed as $y(t) = Ye^{i\omega t}$, where ω is the circular frequency (rad/s) and, therefore, the velocity is $\dot{y}(t) = i\omega Ye^{i\omega t} = i\omega y(t)$ [22]. Substituting for velocity in Eq. (1) yields:

$$T_{max} = \frac{1}{2} m_{eff} \omega^2 y_{max}\, 2. \tag{2}$$

The beam geometry for thin rib machining is depicted in Fig. 1. The fixed-free beam profile is shown, where the thickness has been decreased at its free end by a first machining pass. With each subsequent pass, more material is removed and the profile is changed (i.e., the length of the thin section increases) until the final geometry is obtained with the desired, uniform thickness.

Eq. (2) is updated using the expression for the deflection, $y(x)$, at the beam free end due to a force at the same location:

$$T_{max} = \frac{1}{2} \frac{\left(\frac{m_1}{L_1}\int_0^{L_1} y(x)^2 dx + \frac{m_2}{L_2}\int_{L_1}^{L_1+L_2} y(x)^2 dx\right)}{y_{max}\, 2} \omega^2 y_{max}\, 2, \tag{3}$$

where m_1 and m_2 are the masses of the two sections from Fig. 1 and L_1 and L_2 are the lengths. The integral is split due to the step change in thickness. Equating Eqs. 2 and 3 gives the effective mass.

$$m_{eff} = \frac{m_1}{L_1}\int_0^{L_1} y(x)^2 dx + \frac{m_2}{L_2}\int_{L_1}^{L_1+L_2} y(x)^2 dx \tag{4}$$

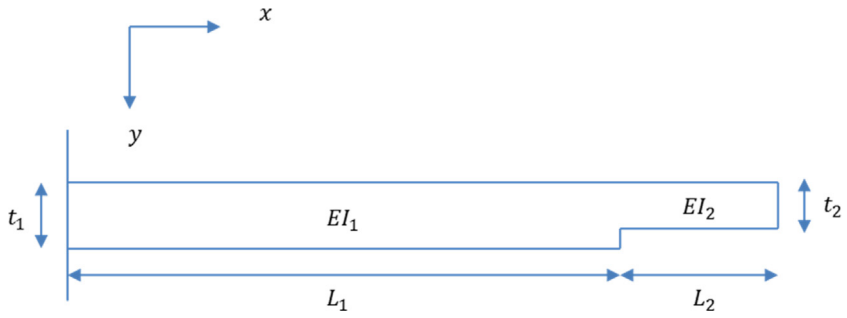

Fig. 1. Beam profile for Rayleigh method modeling. The left end is fixed and the right end is free. The thickness, t, and length, L, are identified for the two sections. The product of the elastic modulus, E, and second moment of area, I, is also listed for the two sections.

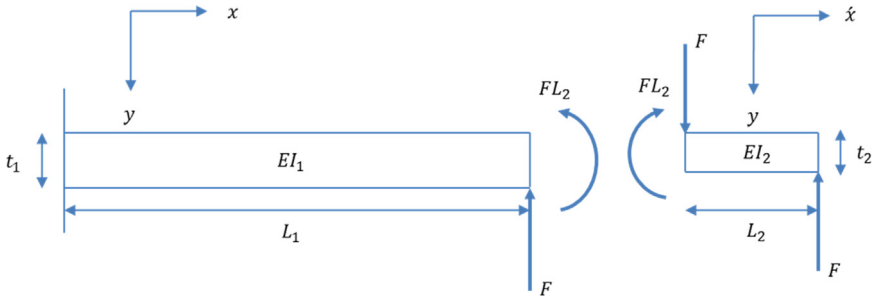

Fig. 2. Beam sections for deflection, $y(x)$, calculation.

The beam deflection is determined by Euler-Bernoulli beam theory. The two beam sections are identified in Fig. 2, where an external force is applied at the beam's free end and the beam is sectioned at the step change in thickness to reveal the internal reaction forces and moments.

The position-dependent deflection of the left section is due to both the force and moment; they are combined by superposition in Eq. (5), where E is the elastic modulus, the second moment of area is $I_1 = \frac{wt_1{}^3}{12}$, and w is the beam width.

$$y(x) = \frac{Fx^3}{6EI_1} - \frac{FL_1x^2}{2EI_1} - \frac{FL_2x^2}{2EI_1} \tag{5}$$

The deflection of the reduced-thickness section, $y(\hat{x})$, is due to the force only, where a change in variable is applied, $\hat{x} = x - L_1$. For this section, the second moment of area is $I_2 = \frac{wt_2{}^3}{12}$.

$$y(\hat{x}) = \frac{F\hat{x}^3}{6EI_2} - \frac{FL_2\hat{x}^2}{2EI_2} \tag{6}$$

It is required that the slope and deflection match at the boundary between the two sections. The slope is described by:

$$\theta(x) = \frac{dy}{dx} = \frac{Fx^2}{2EI_1} - \frac{FL_1x}{EI_1} - \frac{FL_2x}{EI_1}. \tag{7}$$

Evaluating Eq. (7) at $x = L_1$ yields:

$$\theta(L_1) = -\frac{FL_1 2}{2EI_1} - \frac{FL_1L_2}{EI_1}. \tag{8}$$

The resulting beam deflection profile is a piecewise continuous function.

$$y(x) = \begin{cases} \frac{Fx^3}{6EI_1} - \frac{FL_1x^2}{2EI_1} - \frac{FL_2x^2}{2EI_1} & 0 < x \le L_1 \\ y(L_1) + \frac{F(x-L_1)^3}{6EI_2} - \frac{FL_2(x-L_1)^2}{2EI_2} + \theta(L_1)(x-L_1) & L_1 < x \le L_1 + L_2 \end{cases} \tag{9}$$

The stiffness at any point along the beam length is determined using Castigliano's theorem [23]. The bending and shearing strain energy, U, due to a force at the free end is provided in Eq. (10), where G is the shear modulus, A is the cross sectional area (in the direction of the beam width), and $k = 1.2$ for a rectangular cross section. The integrals are again split due to the change in the beam thickness. The shear force, V, and moment, M, are identified in Fig. 3.

$$\begin{aligned} U &= \int_0^{L_1} \frac{M^2dx}{2EI_1} + \int_{L_1}^{L_1+L_2} \frac{M^2dx}{2EI_2} + \int_0^{L_1} \frac{kV^2dx}{2GA_1} + \int_{L_1}^{L_1+L_2} \frac{kV^2dx}{2GA_2} \\ &= \frac{F^2}{2EI_1}\left(\frac{L_1\,33}{} + L_1\,2L_2 + L_1L_2\,2\right) + \frac{F^2}{2EI_2}\left(\frac{L_2\,33}{}\right) + \frac{kF^2}{2GA_1}(L_1) + \frac{kF^2}{2GA_2}(L_2) \end{aligned} \tag{10}$$

The deflection at the free end, where the force is applied, is:

$$y_1 = \frac{\partial U}{\partial F} = \frac{F}{EI_1}\left(\frac{L_1{}^3}{3} + L_1^2L_2 + L_1L_2^2\right) + \frac{F}{EI_2}\left(\frac{L_2{}^3}{3}\right) + \frac{kF}{GA_1}(L_1) + \frac{kF}{GA_2}(L_2), \tag{11}$$

where $A_1 = wt_1$ and $A_2 = wt_2$. The corresponding stiffness is:

$$k_1 = \frac{F}{y_1}. \tag{12}$$

Similarly, the stiffness can be determined at the location of the change in thickness; see Fig. 4. The bending and shearing strain energy for the new force location is described in Eq. (13). The corresponding deflection at the force location, y_2, and stiffness at the force, k_2, are provided in Eqs. (14) and (15). Practically speaking, k_1 and k_2 represent the stiffness at the top of the cut and bottom of the cut, respectively, during the peripheral milling operation.

$$U = \int_0^{L_1} \frac{M^2dx}{2EI_1} + \int_0^{L_1} \frac{kV^2dx}{2GA_1} = \frac{F^2}{2EI_1}\left(\frac{L_1\,33}{}\right) + \frac{kF^2}{2GA_1}(L_1) \tag{13}$$

$$y_2 = \frac{\partial U}{\partial F} = \frac{F}{EI_1}\left(\frac{L_1^3\,3}{}\right) + \frac{kF}{GA_1}(L_1) \tag{14}$$

$$k_2 = \frac{F}{y_2} \tag{15}$$

Given the effective mass and stiffness at the free end, the fundamental natural frequency (in Hz) for the stepped thickness fixed-free beam is calculated using Eq. (16), where the stiffness is expressed in N/m and the effective mass in kg.

$$f_n = \frac{1}{2\pi}\sqrt{\frac{k_1}{m_{eff}}} \tag{16}$$

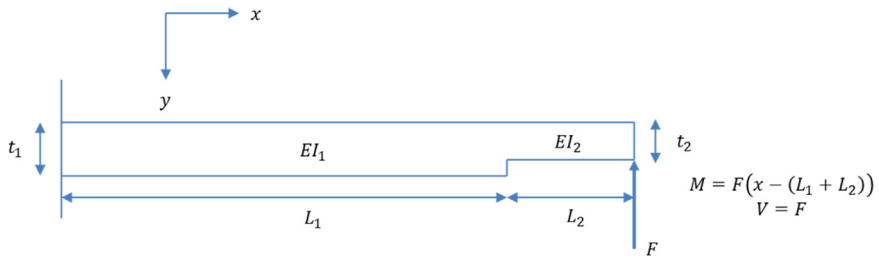

Fig. 3. Moment and shear force for stiffness calculation k_1.

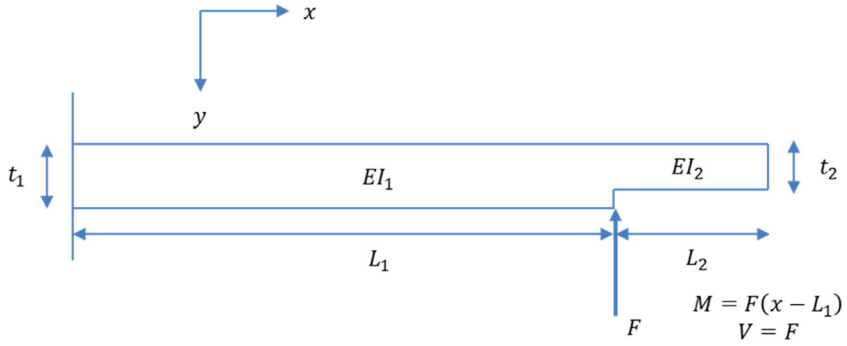

Fig. 4. Moment and shear force for stiffness calculation k_2.

Table 2
Comparison of FE and Raleigh method natural frequency predictions.

L_1(mm)	L_2(mm)	t_1(mm)	t_2(mm)	f_nFE (Hz)	f_nAnalytical (Hz)	% difference
150	0	6	6	217.96	221.33	−1.54
146	4	6	4	221.79	225.45	−1.65
142	8	6	4	225.51	229.49	−1.76
132	18	6	4	234.28	239.16	−2.08
122	28	6	4	242.03	248.06	−2.49
100	50	6	4	253.20	261.72	−3.36
75	75	6	4	248.22	256.73	−3.43
50	100	6	4	219.84	226.48	−3.02
25	125	6	4	180.46	185.61	−2.86
10	140	6	4	157.53	161.99	−2.83
0	150	4	4	145.39	147.55	−1.49

To provide a numerical validation of the approach, finite element (FE) calculations were performed in ANSYS to predict the fixed-free beam receptance at the force location. In this analysis, a unit sinusoidal force was applied at the desired location and the forcing frequency was swept over the desired bandwidth. The corresponding displacement at the force location was measured. Multiple beam geometries were tested where the beam thickness was reduced over a varying length, L_2, to replicate the machining process. In each case, mesh refinement was used to verify convergence and the natural frequency and modal stiffness were extracted by peak picking (a modal fitting procedure [1]) from the predicted direct receptance (i.e., the force and displacement measurement locations were collocated). Natural frequency results are presented in Table 2 and Fig. 5, where the steel beam's elastic modulus was 200 GPa, its width was 20 mm, Poisson's ratio was 0.3, and the density was 7800 kg/m^3. In both Table 2 and Fig. 5, it is observed that the beam's natural frequency first increases and then decreases as material is removed.

The k_1 stiffness results are presented in Table 3 and Fig. 6. The k_2 stiffness results are provided in Table 4 and Fig. 7, where a semilog scale is used due to the dramatic increase in stiffness near the beam base. For comparison purposes, the modal mass extracted from the FE results and m_{eff} predicted by the Rayleigh method are plotted together in Fig. 8.

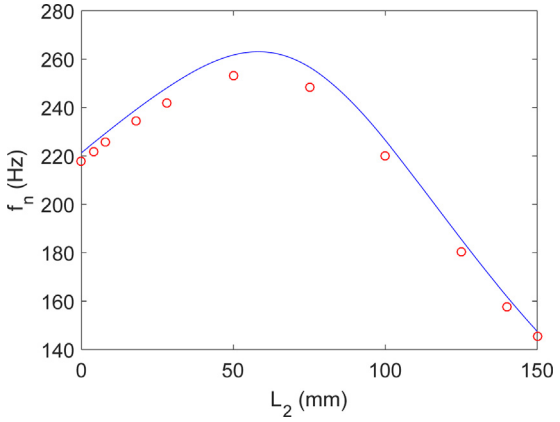

Fig. 5. Graphical comparison of FE (circles) and Raleigh method (line) natural frequency predictions.

2.2. Receptance coupling substructure analysis

RCSA is a frequency domain, analytical procedure used to couple component receptances in order to predict the assembly receptances [22,24]. In this work, the free–free receptances for the machined section of the beam were rigidly coupled to

Table 3
Comparison of FE and Raleigh method k_1 stiffness predictions.

L_1(mm)	L_2(mm)	t_1(mm)	t_2(mm)	k_1 FE (N/m)	k_1Analytical (N/m)	% difference
150	0	6	6	6.5915×10^4	6.3920×10^4	3.03
146	4	6	4	6.6054×10^4	6.3916×10^4	3.24
142	8	6	4	6.6176×10^4	6.3895×10^4	3.45
132	18	6	4	6.6329×10^4	6.3655×10^4	4.03
122	28	6	4	6.6057×10^4	6.2942×10^4	4.72
100	50	6	4	6.2371×10^4	5.8747×10^4	5.81
75	75	6	4	5.1665×10^4	4.9290×10^4	4.60
50	100	6	4	3.8433×10^4	3.7529×10^4	2.35
25	125	6	4	2.7277×10^4	2.6934×10^4	1.26
10	140	6	4	2.2057×10^4	2.1822×10^4	1.06
0	150	4	4	1.9537×10^4	1.8952×10^4	2.99

Table 4
Comparison of FE and Raleigh method k_2 stiffness predictions.

L_1(mm)	L_2(mm)	t_1(mm)	t_2(mm)	k_2 FE (N/m)	k_2Analytical (N/m)	% difference
150	0	6	6	–	–	–
146	4	6	4	7.1162×10^4	6.9314×10^4	2.60
142	8	6	4	7.7001×10^4	7.5333×10^4	2.17
132	18	6	4	9.4891×10^4	9.3763×10^4	1.19
122	28	6	4	1.1945×10^5	1.1873×10^5	0.60
100	50	6	4	2.2295×10^5	2.1540×10^5	3.39
75	75	6	4	6.4489×10^5	5.0946×10^5	21.0
50	100	6	4	3.6000×10^6	1.7088×10^6	52.5
25	125	6	4	7.1920×10^7	1.3230×10^7	81.6
10	140	6	4	3.2515×10^9	1.6864×10^9	94.8
0	150	4	4	–	–	–

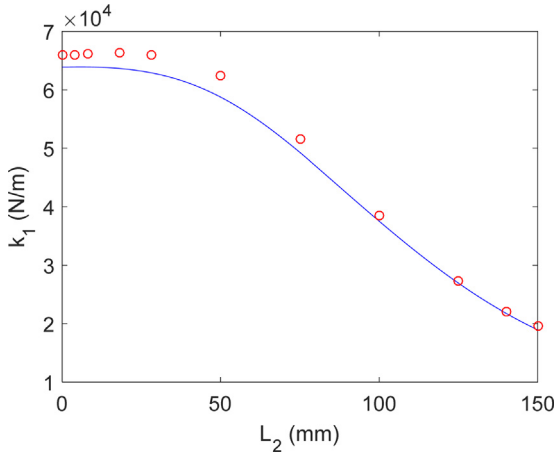

Fig. 6. Graphical comparison of FE (circles) and Raleigh method (line) k_1 stiffness predictions.

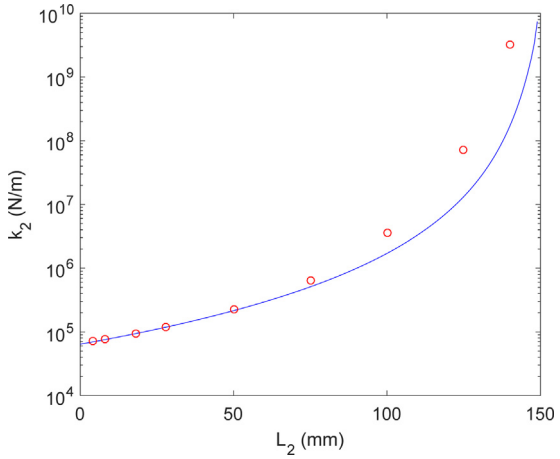

Fig. 7. Graphical comparison of FE (circles) and Raleigh method (line) k_2 stiffness predictions (semilog scale).

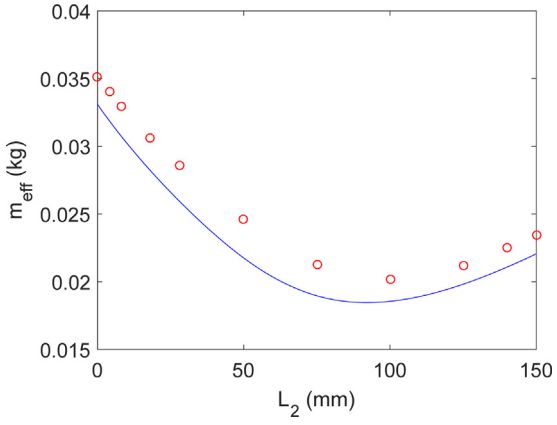

Fig. 8. Graphical comparison of FE (circles) modal mass and Raleigh method (line) m_{eff} predictions.

the remaining (unmachined) fixed-free section; see Fig. 9. Using rigid compatibility and equilibrium conditions, the assembly direct receptances, $H_{11} = \frac{Y_1}{F_1}$ and $H_{22} = \frac{Y_2}{F_2}$, at assembly coordinates Y_1 and Y_2 are written as a function of the component receptances at coordinates 1, 2a, and 2b; see [22] for the derivation. The required direct and cross receptances for the free–free (coordinates 1 and 2a) and fixed-free (coordinate 2b) components are:

- $h_{11} = \frac{y_1}{f_1}$, $h_{12a} = \frac{y_1}{f_{2a}}$, $h_{2a1} = \frac{y_{2a}}{f_1}$, $h_{2a2a} = \frac{y_{2a}}{f_{2a}}$, and $h_{2b2b} = \frac{y_{2b}}{f_{2b}}$, where y_i is the component displacement and f_j is the (internal) component force
- $l_{11} = \frac{y_1}{m_1}, l_{12a} = \frac{y_1}{m_{2a}}, l_{2a1} = \frac{y_{2a}}{m_1}, l_{2a2a} = \frac{y_{2a}}{m_{2a}}$, and $l_{2b2b} = \frac{y_{2b}}{m_{2b}}$, where m_j is the (internal) component moment
- $n_{11} = \frac{\theta_1}{f_1}$, $n_{12a} = \frac{\theta_1}{f_{2a}}$, $n_{2a1} = \frac{\theta_{2a}}{f_1}$, $n_{2a2a} = \frac{\theta_{2a}}{f_{2a}}$, and $n_{2b2b} = \frac{\theta_{2b}}{f_{2b}}$, where θ_i is the component rotation
- $p_{11} = \frac{\theta_1}{m_1}, p_{12a} = \frac{\theta_1}{m_{2a}}, p_{2a1} = \frac{\theta_{2a}}{m_1}, h_{2a2a} = \frac{\theta_{2a}}{m_{2a}}$, and $p_{2b2b} = \frac{\theta_{2b}}{m_{2b}}$.

The assembly receptances are provided in Eqs. (17) and (18) [22].

$$\begin{bmatrix} H_{11} & L_{11} \\ N_{11} & P_{11} \end{bmatrix} = \begin{bmatrix} h_{11} & l_{11} \\ n_{11} & p_{11} \end{bmatrix} - \begin{bmatrix} h_{12a} & l_{12a} \\ n_{12a} & p_{12a} \end{bmatrix} \left(\begin{bmatrix} h_{2a2a} & l_{2a2a} \\ n_{2a2a} & p_{2a2a} \end{bmatrix} + \begin{bmatrix} h_{2b2b} & l_{2b2b} \\ n_{2b2b} & p_{2b2b} \end{bmatrix} \right)^{-1} \begin{bmatrix} h_{2a1} & l_{2a1} \\ n_{2a1} & p_{2a1} \end{bmatrix} \quad (17)$$

$$\begin{bmatrix} H_{22} & L_{22} \\ N_{22} & P_{22} \end{bmatrix} = \begin{bmatrix} h_{2a2a} & l_{2a2a} \\ n_{2a2a} & p_{2a2a} \end{bmatrix} - \begin{bmatrix} h_{2a2a} & l_{2a2a} \\ n_{2a2a} & p_{2a2a} \end{bmatrix} \left(\begin{bmatrix} h_{2a2a} & l_{2a2a} \\ n_{2a2a} & p_{2a2a} \end{bmatrix} + \begin{bmatrix} h_{2b2b} & l_{2b2b} \\ n_{2b2b} & p_{2b2b} \end{bmatrix} \right)^{-1} \begin{bmatrix} h_{2a2a} & l_{2a2a} \\ n_{2a2a} & p_{2a2a} \end{bmatrix} \quad (18)$$

The component receptances can be obtained from measurements or models. Two modeling options are the Euler-Bernoulli and Timoshenko beams. In this work, the one-dimensional Timoshenko beam model was implemented to find the free–free receptances. This requires a numerical solution of the partial differential equation displayed in Eq. (19) [25,26], where $\hat{k}$ is a shape factor that depends on the beam's cross section [27]. To determine the required fixed-free receptances for the L_1 section component, the free–free receptances for this component (obtained from Eq. (19)) were rigidly coupled to a rigid boundary (i.e., zero receptances). Eq. (17) was also applied for this sub-step, where the 2*b* coordinate was assigned to the rigid boundary and the 1 and 2*a* coordinates to the L_1 section component.

$$\left(\frac{\partial^2 y}{\partial t^2} + \frac{EI}{\rho A}\frac{\partial^4 y}{\partial x^4}\right) + \left(\frac{\rho I}{\hat{k}AG}\frac{\partial^4 y}{\partial t^4} + \frac{EI}{\hat{k}AG}\frac{\partial^4 y}{\partial x^2 \partial t^2}\right) - \left(\frac{I}{A}\frac{\partial^4 y}{\partial x^2 \partial t^2}\right) = 0 \quad (19)$$

To provide a numerical validation of the analytical coupling approach, comparisons between the RCSA predictions and ANSYS finite element calculations were completed. Multiple beam geometries were tested where the beam thickness was reduced over a varying length, L_2. In each case, the natural frequency and modal stiffness were extracted by peak picking from the direct receptances. Natural frequency results are presented in Table 5 and Fig. 10, where the steel beam's elastic modulus was 200 GPa, its width was 20 mm, Poisson's ratio was 0.3, and the density was 7800 kg/m^3.

The k_1 stiffness results are presented in Table 6 and Fig. 11. The k_2 stiffness results are provided in Table 7 and Fig. 12.

2.3. Experimental setup

Receptance measurements were completed using a modal hammer (PCB 086C04) to excite the beam and a laser vibrometer (Polytec OFV 5000 controller/OFV 534 laser head) to measure the velocity; see Fig. 13. The direct receptance measurements were performed at the aluminum beam's free end and at the change in

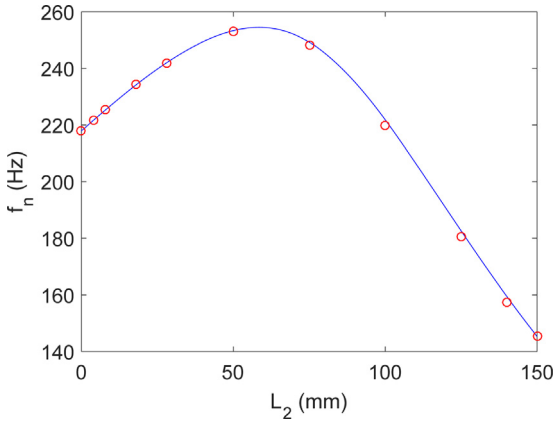

Fig. 10. Graphical comparison of FE (circles) and RCSA (line) natural frequency predictions.

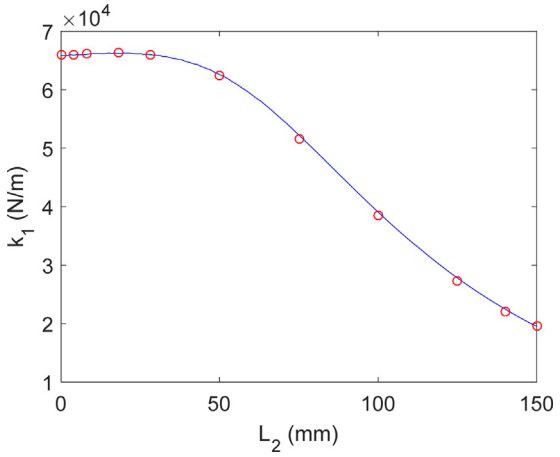

Fig. 11. Graphical comparison of FE (circles) and RCSA (line) k_1 stiffness predictions.

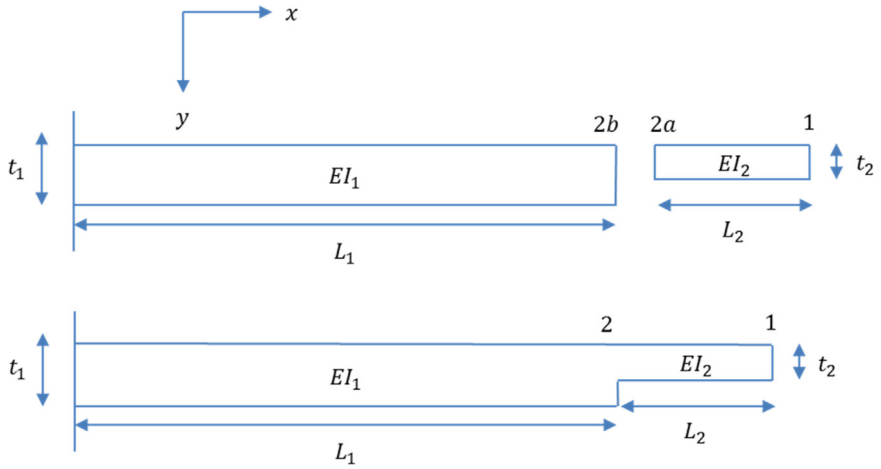

Fig. 9. Beam model for RCSA. (Top) The two components and associated coordinates (1 and 2*a* for the free–free component and 2*b* for the fixed-free component) are identified. (Bottom) The assembly and associated coordinates (1 and 2) are shown.

Table 5
Comparison of FE and RCSA natural frequency predictions.

L_1(mm)	L_2(mm)	t_1(mm)	t_2(mm)	f_nFE (Hz)	f_nAnalytical (Hz)	% difference
150	0	6	6	217.96	217.87	0.04
146	4	6	4	221.79	221.70	0.04
142	8	6	4	225.51	225.42	0.04
132	18	6	4	234.28	234.19	0.04
122	28	6	4	242.03	241.96	0.03
100	50	6	4	253.20	253.37	−0.07
75	75	6	4	248.22	249.26	−0.42
50	100	6	4	219.84	221.82	−0.90
25	125	6	4	180.46	182.63	−1.20
10	140	6	4	157.53	159.54	−1.28
0	150	4	4	145.39	145.34	0.03

Table 6
Comparison of FE and RCSA k_1 stiffness predictions.

L_1(mm)	L_2(mm)	t_1(mm)	t_2(mm)	k_1 FE (N/m)	k_1Analytical (N/m)	% difference
150	0	6	6	6.5915×10^4	6.5758×10^4	0.24
146	4	6	4	6.6054×10^4	6.5894×10^4	0.24
142	8	6	4	6.6176×10^4	6.6016×10^4	0.24
132	18	6	4	6.6329×10^4	6.6185×10^4	0.22
122	28	6	4	6.6057×10^4	6.5969×10^4	0.13
100	50	6	4	6.2371×10^4	6.2577×10^4	−0.33
75	75	6	4	5.1665×10^4	5.2243×10^4	−1.12
50	100	6	4	3.8433×10^4	3.9059×10^4	−1.63
25	125	6	4	2.7277×10^4	2.7779×10^4	−1.84
10	140	6	4	2.2057×10^4	2.2471×10^4	−1.88
0	150	4	4	1.9537×10^4	1.9513×10^4	0.12

Table 7
Comparison of FE and Raleigh method k_2 stiffness predictions.

L_1(mm)	L_2(mm)	t_1(mm)	t_2(mm)	k_2 FE (N/m)	k_2Analytical (N/m)	% difference
150	0	6	6	–	–	–
146	4	6	4	7.1162×10^4	7.0989×10^4	0.24
142	8	6	4	7.7001×10^4	7.6811×10^4	0.25
132	18	6	4	9.4891×10^4	9.4646×10^4	0.26
122	28	6	4	1.1945×10^5	1.1912×10^5	0.28
100	50	6	4	2.2295×10^5	2.2184×10^5	0.50
75	75	6	4	6.4489×10^5	6.3670×10^5	1.27
50	100	6	4	3.6000×10^6	3.5204×10^6	2.21
25	125	6	4	7.1920×10^7	6.9920×10^7	2.78
10	140	6	4	3.2515×10^9	3.1501×10^9	3.12
0	150	4	4	–	–	–

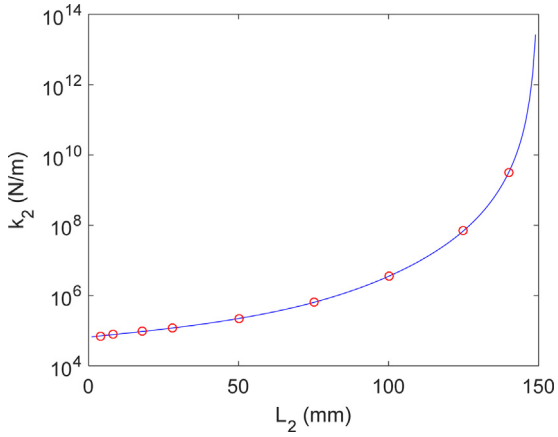

Fig. 12. Graphical comparison of FE (circles) and RCSA (line) k_2 stiffness predictions (semilog scale).

thickness. The length of the reduced thickness section was changed by machining, where a 12.7 mm diameter three-flute solid carbide endmill (approximately 100 mm stickout length) was used (0.1 mm/tooth, 3900 rpm). The beam thickness was removed in 10 mm axial steps with a final radial depth of 1 mm. The beam width was 44.96 mm. Measurements were performed after each machining pass.

3. Results

Because the RCSA predictions matched the finite element results more closely, a comparison between experiments and RCSA receptances was completed for the fundamental bending mode of the aluminum beam displayed in Fig. 13. For the RCSA beams models, the elastic modulus was 69 GPa, Poisson's ratio was 0.33, and the density was 2700 kg/m^3. The natural frequency results are displayed in Table 8 and Fig. 14. The k_1 stiffness results are presented in Table 9 and Fig. 15. The k_2 stiffness results are shown in Table 10 and Fig. 16. In all cases, the parameters were extracted by modal fitting.

3.1. Discussion and application

The results presented in Table 4 deserve further discussion. Table 4 describes the stiffness, k_2, at the location of the step change in the beam thickness. When L_2 is large, there is a short thicker beam supporting a long thinner beam. This stiffness depends on

Table 8
Comparison of experiments and RCSA predictions for natural frequency.

L_1(mm)	L_2(mm)	t_1(mm)	t_2(mm)	f_nExperiment (Hz)	f_nRCSA (Hz)	% difference
80	0	6	6	749	762.4	−1.78
70	10	6	5	776	790.39	−1.85
60	20	6	5	793	810.25	−2.18
50	30	6	5	804	820.04	−2.00
40	40	6	5	800	816.27	−2.03
30	50	6	5	781	795.15	−1.81
20	60	6	5	743	755.49	−1.68
10	70	6	5	691	700.45	−1.37
0	80	5	5	630	636.14	−0.97

Table 9
Comparison of experiments and RCSA predictions for stiffness k_1.

L_1(mm)	L_2(mm)	t_1(mm)	t_2(mm)	k_1Experiment (N/m)	k_1RCSA (N/m)	% difference
80	0	6	6	3.68×10^5	3.34×10^5	9.27
70	10	6	5	3.35×10^5	3.35×10^5	0.04
60	20	6	5	3.51×10^5	3.33×10^5	5.12
50	30	6	5	3.30×10^5	3.25×10^5	1.38
40	40	6	5	3.33×10^5	3.10×10^5	6.99
30	50	6	5	2.89×10^5	2.86×10^5	1.03
20	60	6	5	2.97×10^5	2.57×10^5	13.6
10	70	6	5	2.30×10^5	2.25×10^5	2.14
0	80	5	5	1.93×10^5	1.94×10^5	−0.40

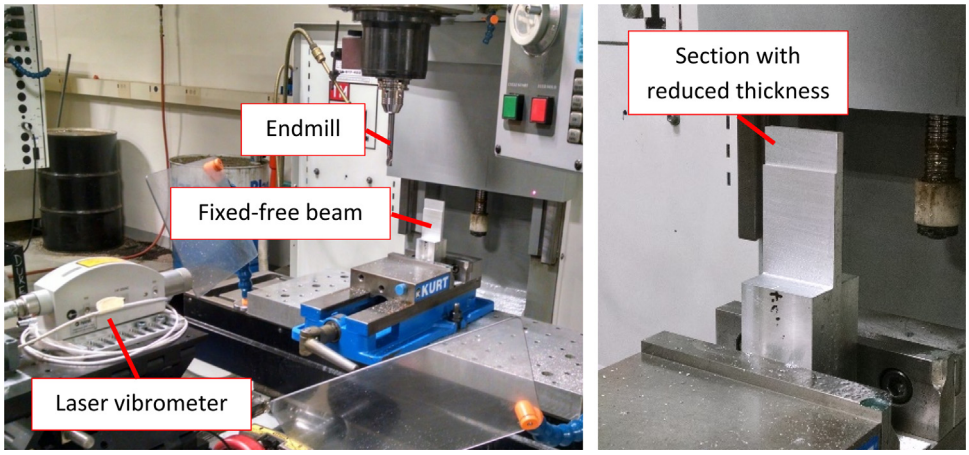

Fig. 13. Experimental setup. (Left) The fixed-free aluminum beam was mounted in a vise which was clamped to the machine table. The laser vibrometer was used to measure the beam response due to a force impact (applied by a modal hammer). (Right) The beam thickness was reduced over a section with a known length and receptance measurements were performed at the top and bottom of the section.

Table 10
Comparison of experiments and RCSA predictions for stiffness k_2.

L_1(mm)	L_2(mm)	t_1(mm)	t_2(mm)	k_2Experiment (N/m)	k_2RCSA (N/m)	% difference
80	0	6	6	–	–	–
70	10	6	5	6.07×10^5	4.87×10^5	19.8
60	20	6	5	9.02×10^5	7.69×10^5	14.7
50	30	6	5	1.72×10^6	1.38×10^6	20.0
40	40	6	5	3.92×10^6	2.97×10^6	24.2
30	50	6	5	1.46×10^7	8.68×10^6	40.6
20	60	6	5	6.21×10^7	4.26×10^7	31.5
10	70	6	5	2.24×10^8	6.80×10^8	−203.5
0	80	5	5	–	–	–

the thicker base portion and, in fact, approaches infinity for a fixed boundary condition (when L_2 is close to the overall beam length). The discrepancy highlights the limitations of analytical models for short, thick beams. The results in Table 4 are based on the Rayleigh method. However, the beam deflection profile used in the analysis is derived from Euler-Bernoulli beam theory. The Euler-Bernoulli beam model neglects rotary inertia, which limits its accuracy for anything but long thin beams and is, therefore, not particularly well-suited to the k_2 modeling. The Euler-Bernoulli beam model is also responsible for the over-prediction of the natural frequency displayed in Fig. 5. The reader may note that the RCSA predictions coupled beam receptances derived from the Timoshenko beam model (Eq. (19)). This improves the agreement with the finite element solution.

From the experimental section, there again appears to be a bias in natural frequency (Fig. 14). In this case the experiments consis-

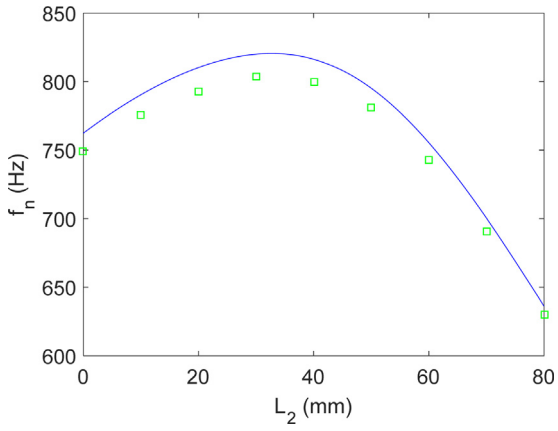

Fig. 14. Graphical comparison of experiments (squares) and RCSA (line) natural frequency predictions.

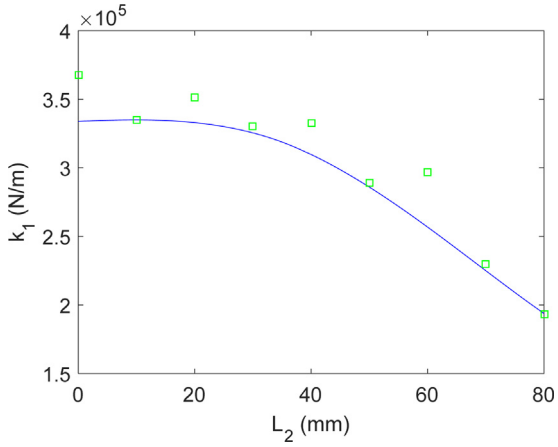

Fig. 15. Graphical comparison of experiments (squares) and RCSA (line) k_1 stiffness predictions.

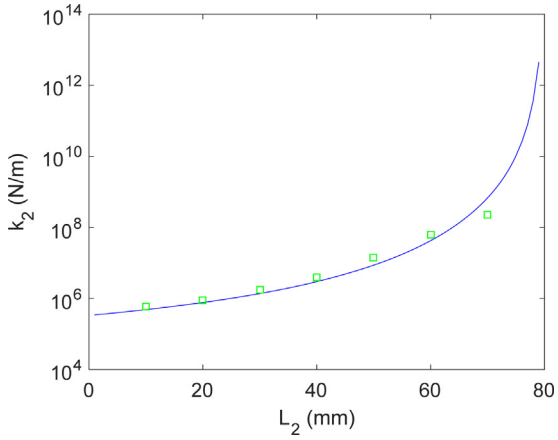

Fig. 16. Graphical comparison of experiments (squares) and RCSA (line) k_2 stiffness predictions (semilog scale).

tently yield a lower natural frequency than the RCSA predictions. This discrepancy could be due to a difference between the actual and nominal material properties used in the analysis. Another possibility is that the model assumed fixed-free boundary conditions. While it was attempted to realize this ideal with the part geometry (i.e., a large base was clamped in a vise; see Fig. 13), it remains a physical approximation.

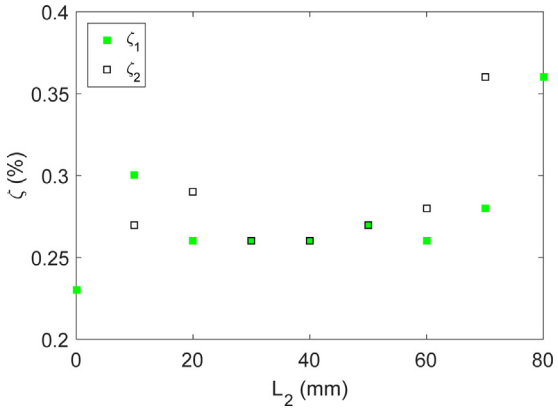

Fig. 17. Experimental damping ratio values from measured direct receptances at the beam's free end, 1, and at the location of the step change in thickness, 2.

In addition to the natural frequency and stiffness values, the dimensionless viscous damping ratios were also extracted from the measured direct receptances. These values are critical because first principle techniques for damping prediction are not available and the damping must, therefore, be included by the modeler based on experience or measurements. The results for the aluminum beam are displayed in Fig. 17 for all nine geometries; damping ratios were extracted from direct receptance measurements at both the free end and thickness change location. The average damping ratio is 0.28% with a standard deviation of 0.04%. The low damping for monolithic structures exacerbates the challenges associated with machining thin, near net shape ribs to produce the final thinner geometries.

In practice, the value of the results presented here are realized when incorporated into a pre-process operating parameter selection algorithm. Based on the machining path and subsequent material removal, the change in beam geometry and, therefore, dynamics can be predicted and the operating parameters can be appropriately selected. For example, using the predicted mass and stiffness together with an informed guess for the associated damping, the corresponding stability limit can be predicted for each machining pass [1]. As the stability limit changes with the beam dynamics, two options are available: 1) the operating parameters can be modified between passes to achieve maximum material removal rates; or 2) the minimum stability limit from all passes can be used to select one set of operating parameters that ensure stable performance throughout the material removal process.

4. Conclusions

Two analytical approaches were presented for predicting thin rib, fixed-free beam dynamics with varying geometries. The first was based on the Rayleigh method and the second on receptance coupling substructure analysis (RCSA). Comparison with finite element calculations showed that the RCSA approach provided better agreement when using the Timoshenko beam model to predict the component receptances.

Experiments were conducted to compare measured fixed-free beam receptances to RCSA predictions. An aluminum beam was machined between receptance measurements to change the thickness. The measured and predicted natural frequencies agreed with an average percent difference of −1.74% for the nine beam profiles. The measured and predicted stiffness values for the fundamental bending mode at the beam's free end agreed with an average percent difference of 4.35% for the nine beam profiles.

Author declaration

This article is not under consideration for publication elsewhere.

Acknowledgements

The authors thank Mr. Kadir Kiran for completing the ANSYS finite element computations and Dr. John Ziegert for helpful discussions. They also gratefully acknowledge partial financial support from Boeing and the National Science Foundation (Grant No. CMMI-1561221).

References

[1] Schmitz T, Smith KS. Machining Dynamics: Frequency Response to Improved Productivity. New York, NY: Springer; 2009.
[2] Budak E, Altintas Y. Modeling and avoidance of static form errors in peripheral milling of plates. Int J Mach Tools Manuf 1995;35:459–76.
[3] Tlusty J, Smith S, Winfough W. Techniques for the use of long slender end mills in high-speed milling. Ann CIRP 1996;45(1):393–6.
[4] Smith S, Dvorak D. Tool path strategies for high speed milling aluminum workpieces with thin webs. Mechatronics 1998;8:291–300.
[5] Ning H, Zhigang W, Chengyu J, Bing Z. Finite element method analysis and control stratagem for machining deformation of thin-walled components. J Mater Process Technol 2003;139:332–6.
[6] Ratchev S, Nikov S, Moualek I. Material removal simulation of peripheral milling of thin wall low-rigidity structures using FEA. Adv Eng Softw 2004;35:481–91.
[7] Ratchev S, Liu S, Huang W, Becker AA. Milling error prediction and compensation in machining of low-rigidity parts. Int J Mach Tools Manuf 2004;44:1629–41.
[8] Bravo U, Altuzarra O, López de Lacalle LN, Sánchez JA, Campa FJ. Stability limits of milling considering the flexibility of the workpiece and the machine. Int J Mach Tools Manuf 2005;45:1669–80.
[9] Ratchev S, Liu S, Becker AA. Error compensation strategy in milling flexible thin-wall parts. J Mater Process Technol 2005;162–163:673–81.
[10] Thevenot V, Arnaud L, Dessein G, Cazenave-Larroche G. Influence of material removal on the dynamic behavior of thin-walled structures in peripheral milling. Mach Sci Technol 2006;10(3):275–87.
[11] Mañé I, Gagnol V, Bouzgarrou BC, Ray P. Stability-based spindle speed control during flexible workpiece high-speed milling. Int J Mach Tools Manuf 2008;48:184–94.
[12] Rai JK, Xirouchakis P. Finite element method based machining simulation environment for analyzing part errors induced during milling of thin-walled components. Int J Mach Tools Manuf 2008;48:629–43.
[13] Seguy S, Dessein G, Arnaud L. Surface roughness variation of thin wall milling, related to modal interactions. Int J Mach Tools Manuf 2008;48:261–74.
[14] Adetoro OB, Wen PH, Sim WM, Vepa R. Stability lobes prediction in thin wall machining. In: Proceedings of the World Congress on Engineering 2009 Vol I. 2009.
[15] Chen W, Xue J, Tang D, Chen H, Qu S. Deformation prediction and error compensation in multilayer milling processes for thin-walled parts. Int J Mach Tools Manuf 2009;49:859–64.
[16] Gang L. Study on deformation of titanium thin-walled part in milling process. J Mater Process Technol 2009;209:2788–93.
[17] Arnaud L, Gonzalo O, Seguy S, Jauregi H, Peigné G. Simulation of low rigidity part machining applied to thin-walled structures. Int J Adv Manuf Technol 2011;54:479–88.
[18] Izamshah R, Mo JPT, Ding S. Hybrid deflection prediction on machining thin-wall monolithic aerospace components. Proc. IMechE Part B: J Eng Manuf 2011;226:592–605.
[19] Smith S, Wilhelm R, Dutterer B, Cherukuri H, Goel G. Sacrificial structure preforms for thin part machining. CIRP Ann – Manuf Technol 2012;61:379–82.
[20] Polishetty A, Goldberg M, Littlefair G, Puttaraju M, Patil P. A preliminary assessment of machinability of titanium allow Ti 6Al 4 V during thin wall machining using trochoidal milling. Proced Eng 2014;97:357–64.
[21] Meirovitch L. Principles and Techniques of Vibrations. Upper Saddle River NJ: Prentice Hall; 1997.
[22] Schmitz T, Smith KS. Mechanical Vibrations: Modeling and Measurement. New York NY: Springer; 2012.
[23] Boresi A, Schmidt R, Sidebottom O. Advanced Mechanics of Materials. 5th ed. New York, NY: John Wiley & Sons, Inc.; 1993.
[24] Bishop RED, Johnson DC. The Mechanics of Vibration. Cambridge UK: Cambridge University Press; 1960.
[25] Weaver Jr W, Timoshenko P, Young D. Vibration Problems in Engineering. 5th ed. New York, NY: John Wiley and Sons; 1990.
[26] Schmitz T, Duncan GS. Three-component receptance coupling substructure analysis for tool point dynamics prediction. J Manuf Sci Eng 2005;127(4):781–90.
[27] Hutchinson J. Shear coefficients for Timoshenko beam theory. J Appl Mech 2001;68:87–92.